



HAL
open science

Influence of Fe doping on the Yb valence state and the magnetic structures in HoFe₆Sn₆-type YbMn_{6–y}FeySn₆ alloys ($y \leq 1.00$)

A. Magnette, L. Eichenberger, L. V. B. Diop, G. Venturini, L. Nataf, F. Baudalet, A. Vernière, T. Mazet

► To cite this version:

A. Magnette, L. Eichenberger, L. V. B. Diop, G. Venturini, L. Nataf, et al.. Influence of Fe doping on the Yb valence state and the magnetic structures in HoFe₆Sn₆-type YbMn_{6–y}FeySn₆ alloys ($y \leq 1.00$). *Journal of Alloys and Compounds*, 2021, 875, pp.160091. 10.1016/j.jallcom.2021.160091 . hal-03325706

HAL Id: hal-03325706

<https://hal.science/hal-03325706>

Submitted on 25 Aug 2021

HAL is a multi-disciplinary open access archive for the deposit and dissemination of scientific research documents, whether they are published or not. The documents may come from teaching and research institutions in France or abroad, or from public or private research centers.

L'archive ouverte pluridisciplinaire **HAL**, est destinée au dépôt et à la diffusion de documents scientifiques de niveau recherche, publiés ou non, émanant des établissements d'enseignement et de recherche français ou étrangers, des laboratoires publics ou privés.

Influence of Fe doping on the Yb valence state and the magnetic structures in HoFe₆Sn₆-type YbMn_{6-y}Fe_ySn₆ alloys ($y \leq 1.00$)

A. Magnette¹, L. Eichenberger¹, L.V.B. Diop¹, G. Venturini^{1†}, L. Nataf², F. Baudalet², A. Vernière¹, T. Mazet^{1*}

¹ Université de Lorraine, CNRS, IJL, F-54000 Nancy, France

² Synchrotron SOLEIL, UR1 CNRS, Saint-Aubin BP 48, 91192 Gif-sur-Yvette, France

† 1954-2019

* Corresponding author: *E-mail address:* thomas.mazet@univ-lorraine.fr

Abstract. We determine the magnetic structures of HoFe₆Sn₆-type (*Immm*) YbMn_{6-y}Fe_ySn₆ alloys ($y = 0.25, 0.50, 0.75$ and 1.00) from powder neutron diffraction experiments. The valence state and local magnetism of Yb are investigated using X-ray Near Edge Spectroscopy (XANES) and X-ray Magnetic Circular Dichroism (XMCD) at the Yb L₃ edge. The mean Yb valence decreases upon Fe doping (from $\nu \sim 2.66$ down to $\nu \sim 2.46$) and there is no $4f$ Yb magnetism throughout the series. The Fe for Mn substitution leads to change in the spins arrangement of the $3d$ sublattice by reinforcing antiferromagnetic exchange interactions without significant change in $T = \text{Mn/Fe}$ moment magnitude ($m \sim 2.35 \mu_B$). The ground state of the alloy with $y = 0.25$ is ferromagnetic whilst Fe richer alloys are helimagnets with wave-vector $\mathbf{k} = 0, q_y, 0$. The turn-angle increase upon Fe doping manifests by a mitigation of the Yb L₃ dichroic effect, solely due to hybridization between its $5d$ states and the self-polarized $3d$ states of T.

Keywords: Intermetallics; Magnetic structures; Intermediate valence

1. Introduction

The study of quantum critical effects and more generally of the physical properties of “strange metals” are currently of high interest in condensed-matter physics [1-3]. In rare-earth based intermetallics, heavy-fermion behaviors and quantum criticality are mainly investigated in materials where Ce or Yb are alloyed with non-magnetic elements [4,5]. Quantum critical effects are then generally perceived at low temperature near the magnetic instability of almost trivalent $4f$ element. Recently, we showed that the situation is somewhat different in YbMn₆Ge_{6-x}Sn_x where intermediate valent Yb is alloyed with a ferromagnetic Mn sublattice [6-10]. In this series of compounds, the Yb magnetic ordering temperature reaches record values up to $T_{Yb} = 125$ K [6,9], the Yb magnetic instability

occurs for far from trivalent Yb ($v \sim 2.73$) and signatures of quantum criticality persists up to room temperature [10]. These unusual phenomena have been ascribed to the strong Mn-Yb exchange interactions [7-10], i.e. to the strong exchange field H_{ex} [11] generated at the Yb site by the neighboring Mn moments.

In 1:6:6 phases, Fe is known to promote antiferromagnetic interlayer exchange interactions [12,13]. To better delineate the role of H_{ex} , we aim at investigating the effect of Fe doping in $YbMn_6Ge_{6-x}Sn_x$ and the ensuing expected reduction of H_{ex} . We started by investigating the effect of Fe doping in $YbMn_6Sn_6$, where intermediate valent Yb ($v \sim 2.59$) is non-magnetic [14], for an understanding of the influence of Fe doping on the magnetism of the 3d sublattice and Yb valence state without the complications due to Yb magnetic ordering,

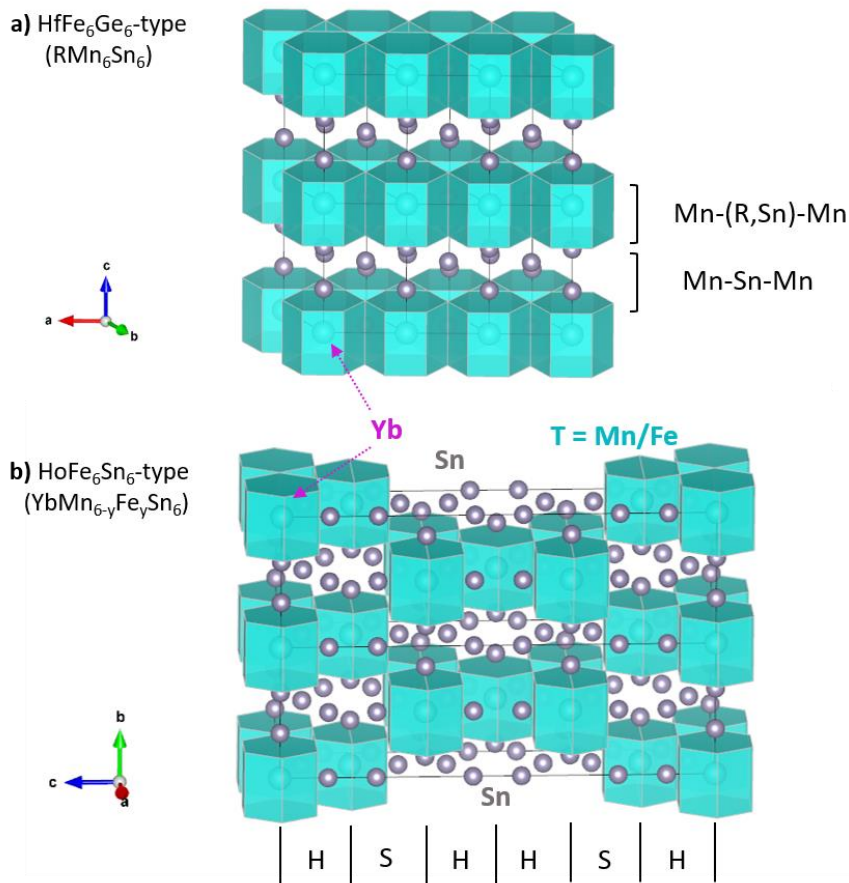


Fig. 1. (color online) (a) HfFe₆Ge₆-type of structure ($P6/mmm$) of most RMn₆Sn₆ compounds and (b) HoFe₆Sn₆-type of structure ($Immm$) of YbMn_{6-y}Fe_ySn₆. The perfect kagomé planes of T atoms in HfFe₆Ge₆ are slightly corrugated in HoFe₆Sn₆. In both cases, the R atoms occupy the center of half the hexagonal prisms of T atoms; the other half contains only Sn atoms. The hexagonal structure can be described as an alternative stacking of Mn-(R,Sn)-Mn and Mn-Sn-Mn slabs. The orthorhombic cell can be viewed as intergrowth of HfFe₆Ge₆ (H) and ScFe₆Ga₆ (S) blocs.

In a previous paper [15], we determined the crystal and magnetic properties of $\text{YbMn}_{6-y}\text{Fe}_y\text{Sn}_6$. Most of the RMn_6Sn_6 compounds crystallize in the hexagonal HfFe_6Ge_6 type structure ($P6/mmm$, a_h , c_h). In this crystal structure, the Mn kagomé planes define an array of edge-sharing hexagonal prisms, half of which being centered by R atoms. The Sn atoms occupy the remaining hexagonal prisms in form of dumbbells and center the trigonal prisms formed by two kagomé planes. The $\text{YbMn}_{6-y}\text{Fe}_y\text{Sn}_6$ alloys were found to adopt the orthorhombic HoFe_6Sn_6 -type of structure, based on the orthohexagonal cell ($Immm$, $a = a_h$, $b = c_h$, $c = 3\sqrt{3}a_h$ [16]), where part of the Yb-filled hexagonal prisms are shifted in an orderly fashion of $b/2 = c_h/2$ from their ideal position (Fig. 1). As a result, some Yb-filled hexagonal prisms are only corner-sharing and the kagomé layers are slightly corrugated. In $\text{YbMn}_{6-y}\text{Fe}_y\text{Sn}_6$, the cell volume shrinks upon Fe doping as $\frac{\Delta V}{V} \sim 0.144\Delta y$ [15]. In YbMn_6Sn_6 , the Mn sublattice is purely ferromagnetic with $T_C \sim 300$ K [17]. The partial substitution of Fe for Mn has little influence on the ordering temperature but yields the appearance of an antiferromagnetic-like phase at low temperature [15]. The latter develops upon Fe doping to cover almost the entire ordered temperature range for $y = 1.00$.

In the present work, we complete our former study on $\text{YbMn}_{6-y}\text{Fe}_y\text{Sn}_6$ ($y \leq 1.00$) [15] using powder neutron diffraction as well as X-ray Near Edge Spectroscopy (XANES) and X-ray Magnetic Circular Dichroism (XMCD) measurements at the Yb L_3 edge. This work is organized as follows. Section 2 deals with experimental details. In section 3 we present the experimental results, which are discussed in section 4 before a short conclusion.

2. Synthesis and Experimental details

The samples investigated here are those used in Ref. [15] where details about the synthesis procedure can be found. They are almost single-phase with low level (< 5 wt. %) of well identified impurities: Yb_2O_3 , β -Sn and MnSn_2 .

The X-ray Absorption Near Edge Structure (XANES) and X-ray Magnetic Circular Dichroism (XMCD) at the Yb L_3 edge were carried out at the ODE beamline of the SOLEIL synchrotron (Saint-Aubin, France) [18]. Absorption spectra were recorded with dispersive mode at 300 K and 5 K in a He circulating cryostat using a position sensitive CCD detector. Cu foil absorption spectrum was needed to correlate position (pixels) and energy (eV). The Yb valence was extracted from the XANES spectra as described in Ref. [14]. The XMCD spectra were obtained at 5 K as the difference of the XANES intensities recorded under an applied field of ~ 1.3 T aligned parallel and antiparallel to the beam while keeping constant the beam helicity.

Powder neutron diffraction experiments were performed at the Institut Laue Langevin (Grenoble, France) using the high-intensity two-axis diffractometer D1B ($\lambda = 2.52$ Å, step of 0.1°). Long duration patterns were recorded at 2 K and 310 K. Rapid thermal scans were carried out between these two temperatures. The data were analyzed using the Rietveld method with the Fullprof program [19].

The shape of the diffraction peaks was fitted using a pseudo-Voigt function. Besides the peak profile parameters, the refinements comprised scale factor, zero shift, cell parameters, crystallographic position parameters and the Mn/Fe occupancy. In the magnetically ordered state, the magnitude and orientation of the moments were treated as additional free parameters. The nuclear contribution from the impurities were taken into account. The overall temperature factor B_{ov} was fixed to 1.0 and 0.1 \AA^2 at 310 K and 2 K, respectively. The R_{wp} and R_e Rietveld agreement factors used here correspond, respectively, to the weight profile and expected factors [20] while R_n and R_m are the Bragg agreement factors calculated for, respectively, the nuclear and magnetic contributions to the diffraction pattern.

3. Experimental results (and discussion)

3.1. XANES and XMCD

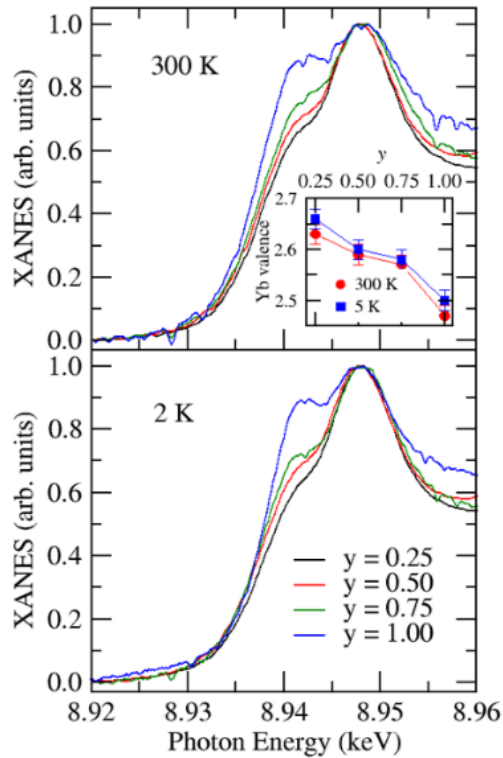


Fig. 2. (color online) Yb L_3 XANES spectra of $\text{YbMn}_{6-y}\text{Fe}_y\text{Sn}_6$ ($y = 0.25, 0.50, 0.75, 1.00$) at 300 K and 5 K. The inset shows the composition dependence of the fitted Yb valence.

The Yb L_3 edge XANES measurements were used to investigate the average Yb valence. The spectra recorded at 300 K (in the paramagnetic state) and at 5 K are shown in Fig. 2. They consist of a main structure near 8.948 keV and a shoulder near 8.940 keV that correspond, respectively, to transitions from the initial Yb intermediate valent state to the final states of mainly $2p^54f^3$ (trivalent) and $2p^54f^4$ (divalent) character. The spectra are thus indicative of Yb being in an intermediate valence state. The spectra were fitted using two pseudo-Voigt functions for the two structures and two arctangent-type step

functions due to the $2p_{3/2} \rightarrow$ continuum transitions. The weight of each valence configuration ($4f^{13}$ and $4f^{14}$) in the initial valence state is proportional to the peaks surface area S_3 and S_2 . The mean Yb valence was derived from $(2S_2+3S_3)/(S_2+S_3)$. The estimated accuracy on the Yb valence is ± 0.02 .

Upon Fe doping, there is a spectral weight transfer from the trivalent component towards the divalent one at both temperatures. The Fe for Mn substitution may a priori alter the Yb valence via three mechanisms: change in chemical pressure due to lattice contraction, modification of the electronic structure and variation of the exchange field. The extracted mean Yb valence values are plotted as a function of y – the Fe content – in the inset of Fig. 2. The Yb valences are found to lie in the $2.46 < \nu < 2.66$ range, a little lower than those inferred from cell volumes [15], and decrease upon increasing the iron content. At 300 K, the alloys are in the paramagnetic state where only a residual exchange field might persist due to local effects. Hence, the Yb valence variation at 300 K arises predominantly from the chemical pressure effect and change in the band structure. Since the Yb valence decreases despite the lattice shrinkage, it can be concluded that the Yb valence change upon Fe doping is dominated by electronic structure modifications. The low-temperature Yb valence values at 5 K in the magnetically ordered state, follows the same trend with little higher valence values. That is further discussed in section 4. In all cases, the mean Yb valence is lower than the ‘magnetic limit’ value of $\nu \sim 2.73$ found in $\text{YbMn}_6\text{Ge}_{6-x}\text{Sn}_x$ below which Yb is no longer magnetic [9,10].

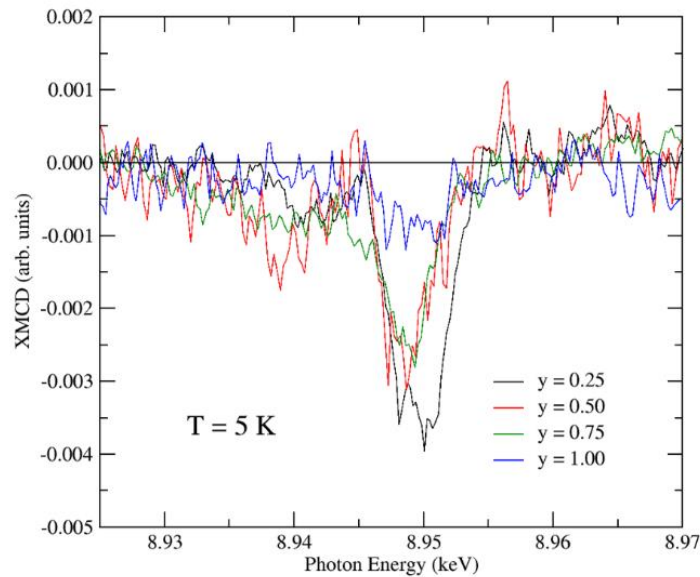


Fig. 3. (color online) Yb L_3 XMCD spectra of $\text{YbMn}_{6-y}\text{Fe}_y\text{Sn}_6$ ($y = 0.25, 0.50, 0.75, 1.00$) at 5 K

The Yb L_3 edge XMCD experiments were carried out at 5 K to gain information on the local magnetism of Yb. Sum rules do not apply to the L_3 edge of rare-earths so that only qualitative information can be extracted [21]. The XMCD spectra are shown in Fig. 3. They confirm the lack of Yb $4f$ magnetism inferred from magnetization data [15]. The spectra only comprise a weak and negative

signal near $E \sim 8.950$ keV, which is due to spin-dependent hybridization between the $5d$ states of Yb and the self-polarized $3d$ states of the $T = \text{Mn/Fe}$ transition metal sublattice [22]. In presence of $4f$ magnetism, the spectra would in addition comprise two more intense peaks of opposite sign: a positive one of dipolar origin and a negative one from quadrupolar origin near $E \sim 8.937$ keV [10]. The weak negative signal decreases in magnitude upon Fe doping, suggesting a reduction in the polarization of the $5d$ states of Yb by the T sublattice.

3.2. Neutron diffraction

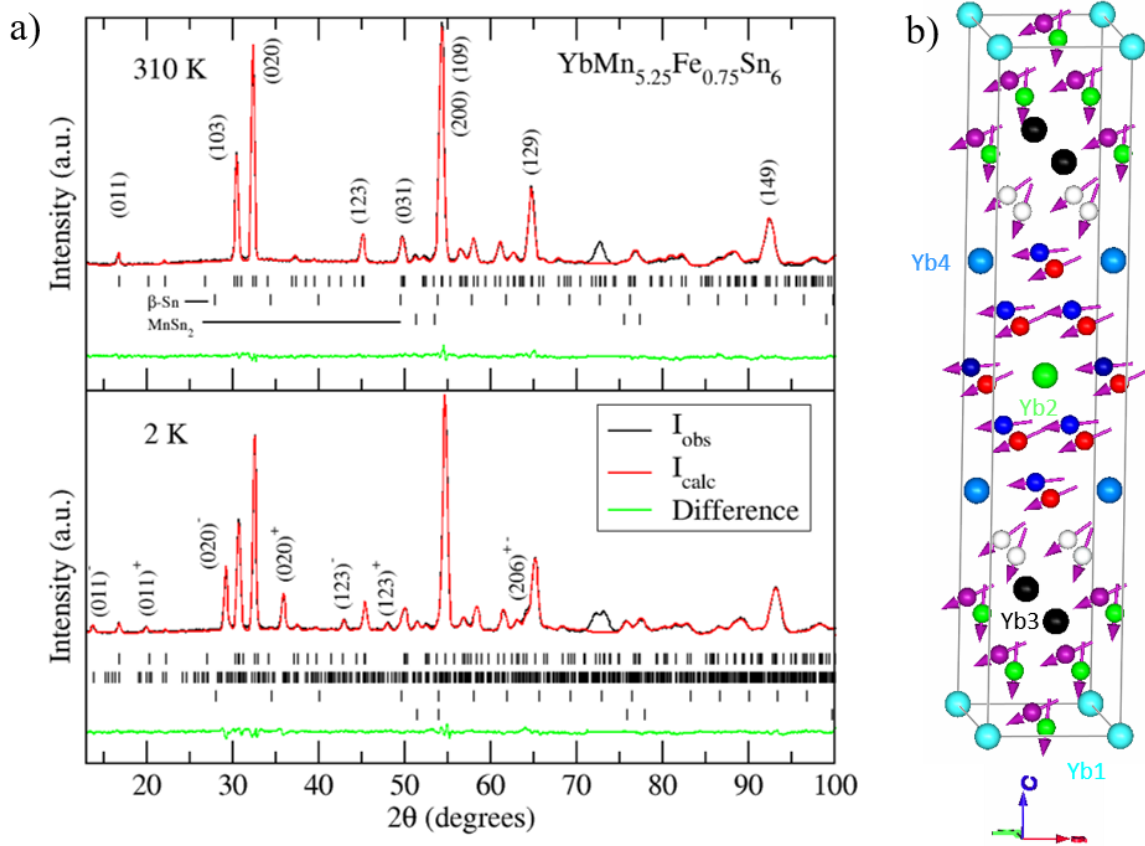


Fig. 4. (color online) (a) Neutron diffraction patterns of $\text{YbMn}_{5.25}\text{Fe}_{0.75}\text{Sn}_6$ at 310 K and 2 K. The angular region around $2\theta \sim 72^\circ$ was excluded from the refinements due to contributions from the cryostat. (b) Schematic representation of the low-temperature helimagnetic structure of $\text{YbMn}_y\text{Fe}_{1-y}\text{Sn}_6$ ($y = 0.50, 0.75, 1.00$). For the sake of clarity, the Sn atoms are not shown and the different groups of T atoms with identical phase are represented using different colors (ϕ_1 : purple, ϕ_3 : green, ϕ_2 : blue, ϕ_4 : red; see text). The T atoms in $8k$ position, taken as the phase origin, are drawn in white.

The neutron patterns recorded in the paramagnetic state at 310 K comprise only diffraction peaks originating from the HoFe_6Sn_6 -type phase and tiny peaks arising from the impurities whose nuclear contribution was taken into account during the refinements (Fig. 4a). To avoid a too large number of

intensity dependent parameters, only the y -component of the T $4h$, $8l$ and $16o$ sites as well as that of Sn $4g$ and $8l$ were let free to vary. The other coordinates were kept fixed to their values deduced from the atomic positions in the hexagonal subcell. Further, the Fe atoms were assumed to distribute equally over the four available transition metal sites. This resulted in satisfactory fits that yield iron contents close to the nominal ones (Table 1). No supplementary line appears in the neutron diffraction patterns of the alloy with $y = 0.25$ upon cooling down to 2 K. Only weak intensity adds at the top of some nuclear peaks, in agreement with the pure ferromagnetic behavior observed from DC magnetization [15]. The best refinements were obtained considering no magnetic moment on Yb, as expected from the XMCD data, and ferromagnetic (010) kagomé T layers ferromagnetically coupled along the b axis, with the T moments lying in the (010) planes. At 2 K, the T = Mn/Fe moment magnitude refines to $m = 2.40(3) \mu_B$, close to that found in the YbMn_6Sn_6 parent compound ($m \sim 2.35 \mu_B$ [17]).

Table 1

Main refined structural and magnetic parameters of $\text{YbMn}_{6-y}\text{Fe}_y\text{Sn}_6$ from neutron data.

	$y = 0.25$		$y = 0.50$		$y = 0.75$		$y = 1.00$	
	310 K	2 K	310 K	2 K	310 K	2 K	310 K	2 K
$y_{\text{Sn}8l}$	0.166(2)	0.165(3)	0.166(2)	0.163(4)	0.168(2)	0.171(1)	0.169(2)	0.170(1)
$y_{\text{Sn}4g}$	0.341(5)	0.339(5)	0.341(4)	0.337(7)	0.342(4)	0.345(3)	0.345(3)	0.345(3)
$y_{\text{T}16o}$	0.247(1)	0.251(1)	0.247(1)	0.249(1)	0.247(2)	0.245(1)	0.245(2)	0.245(2)
$y_{\text{T}8l}$	0.246(3)	0.254(3)	0.252(3)	0.253(3)	0.251(4)	0.246(3)	0.257(5)	0.250(4)
$y_{\text{T}4h}$	0.255(3)	0.253(3)	0.257(3)	0.254(4)	0.255(4)	0.251(4)	0.243(5)	0.244(5)
q_y (r.l.u.)	-	0	-	0.128(1)	-	0.199(1)	-	0.251(1)
occ. Fe	0.038(4)	0.034(7)	0.074(4)	0.064(6)	0.128(4)	0.119(4)	0.167(4)	0.163(4)
m (μ_B)	-	2.40(3)	-	2.28(3)	-	2.36(2)	-	2.28(2)
ϕ_1 ($^\circ$)	-	-	-	-41(8)	-	-52(6)	-	-36(5)
ϕ_2 ($^\circ$)	-	-	-	12(8)	-	11(5)	-	5(4)
ϕ_3 ($^\circ$)	-	-	-	-33(8)	-	-32(5)	-	-14(4)
ϕ_4 ($^\circ$)	-	-	-	-15(8)	-	-15(5)	-	-26(5)
R_n, R_m	7.6,-	6.5, 2.5	5.8, -	6.5, 14.6	7.0, -	3.7, 14.2	7.8, -	4.4, 8.6
(%)								
R_{wp}, R_e (%)	8.9, 0.5	7.5, 0.4	8.4, 1.5	10.3, 1.4	7.8, 1.0	7.5, 0.7	9.6, 1.3	7.9, 1.2

The neutron patterns of the Fe richer alloys ($y = 0.50, 0.75$ and 1.00) evolve in a similar manner upon decreasing temperature. There is first a ferromagnetic region where magnetic intensity increases upon cooling on the top of some nuclear peaks. Then, this ferromagnetic intensity goes to zero and a new set of satellites appears below $T_t \sim 120$ K, ~ 215 K and ~ 270 K, respectively. This is reminiscent

of the neutron patterns of the double flat spiral magnetic structure found in many Mn-based hexagonal HfFe_6Ge_6 -type 1:6:6 compounds [6,14,23,24] where the orientation of the Mn moment \mathbf{m}_{Mn} in the kagomé planes is given by: $\mathbf{m}_{\text{Mn}} = m_{\text{Mn}} \cos(\mathbf{k} \cdot \mathbf{R}_n + \varphi)\mathbf{u} + m_{\text{Mn}} \sin(\mathbf{k} \cdot \mathbf{R}_n + \varphi)\mathbf{v}$. Here, \mathbf{u} and \mathbf{v} are orthogonal basis vectors in the hexagonal plane, \mathbf{R}_n is the position vector in the n^{th} chemical cell and φ is the phase angle [25]. In $\text{YbMn}_{6-y}\text{Fe}_y\text{Sn}_6$, the set of satellites can be fully indexed using an incommensurate wave vector $\mathbf{k} = 0, q_y, 0$ (Fig. 4a). To best of our knowledge, incommensurate arrangements of the T magnetic moments have not yet been observed in 1:6:6 phases crystallizing with the HoFe_6Sn_6 -type or with one other of the large cells described in [15]. The q_y component increases with the Fe content and upon cooling (Fig. 5).

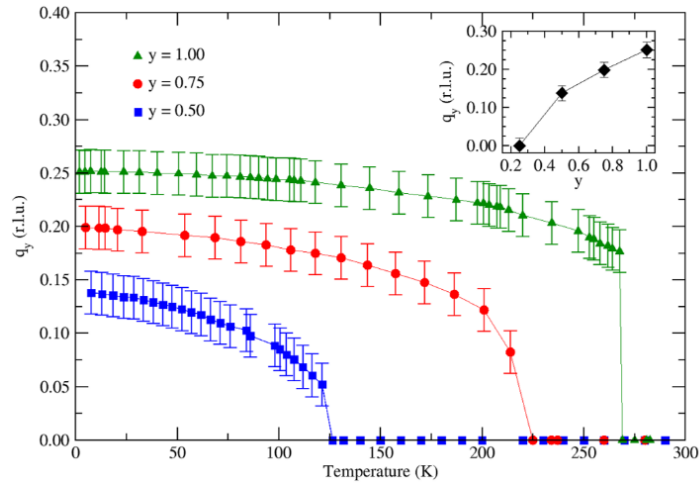


Fig. 5. (color online) Temperature dependence of the q_y component of the wave vector of the helimagnetic structure of $\text{YbMn}_{6-y}\text{Fe}_y\text{Sn}_6$. The inset shows the composition dependence at 2 K

The refinements of the 2 K patterns were carried out with no magnetic moment on Yb, as observed from XMCD data. In all cases, the T magnetic moment of the various crystallographic sites were constrained to be of identical magnitude. First attempts to refine the low-temperature diffraction patterns were conducted using a unique phase shift between the T moments in the $y \sim 0.25$ and $y \sim 0.75$ layers, respectively. This resulted in unsatisfactory fits, notably because the calculated intensity for the $(011)^-$ and $(011)^+$ satellites is then significantly too low. For these incommensurate peaks to have a strong enough intensity, it is necessary to introduce phase shifts between the T moments within a given $y \sim 0.25$ (or $y \sim 0.75$) deformed kagomé plane.

The T moments with identical phase angle were grouped based on crystal-chemistry considerations. In helimagnetic HfFe_6Ge_6 -type RMn_6Sn_6 compounds, the rotation of the Mn moments is larger through the Mn-(R,Sn)-Mn slabs of R-filled prisms than through the Mn-Sn-Mn slabs. The orthorhombic HoFe_6Sn_6 -type structure of $\text{YbMn}_{6-y}\text{Fe}_y\text{Sn}_6$ can also be described as a stacking of H blocs (related to the HfFe_6Ge_6 cell) and S blocs (related to the ScFe_6Ga_6 cell [26]) with the following sequence H-S-H-H-S-H (see Fig. 1) [15]. In the H blocs, the Yb-filled prisms are edge-sharing while they are

corner-sharing in the S blocs. The phase angles were introduced to take into account the change in turn-angle through the Yb filled prisms. The moments of the corner-sharing T atoms within the S blocs (i.e. those in $8k$ position) were taken as the phase origin. Four different phase angles were chosen for the moments on the three remaining T sites ($16o$, $8l$ and $4h$). Two phase angles (φ_1 and φ_3) for, respectively, the T moments in the $y \sim 0.25$ and $y \sim 0.75$ hexagonal layers of the filled-prisms with Yb in $y = 0$. Two other phase angles (φ_2 and φ_4) for the shifted hexagonal prisms surrounding Yb in $y = \frac{1}{2}$ (Fig. 4b).

The refinements carried out under this assumption resulted in quite satisfactory fits, keeping in mind the low signal/noise ratio of the magnetic satellites, with magnetic R-factors R_m in the 8-15 % range. The main refined magnetic parameters are given in Table 1. For the three richest Fe alloys, the T moment is found close to $\sim 2.30 \mu_B$. The corresponding magnetic structure is depicted in Fig. 4b. The rotation angles can be calculated from the refined y -coordinates, q_y and phase shifts values. An important consequence of introducing phase shifts for T moments with close y coordinate is that the moments within a given corrugated kagomé plane are no longer collinear and can make an angle up to $\sim 60^\circ$ for T atoms pertaining to two non-contiguous H blocs. To best of our knowledge, this is the first time that non-collinear arrangement of the magnetic moments are observed in the kagomé plane of 1:6:6 compounds. Due to the phase shifts introduced to refine the neutron data, the body-centered symmetry is lost and each of the two Yb site splits into two magnetic sub-sites. The Yb $2a$ position splits into Yb_1 ($0, 0, 0$) and Yb_2 ($1/2, 1/2, 1/2$) while Yb $4j$ splits into Yb_3 ($1/2, 0, \pm 0.16$) and Yb_4 ($0, 1/2, \pm 0.33$). The mean χ_i turn-angle ($i = 1, 2, 3$ or 4) through Yb filled hexagonal prisms increases upon Fe doping to reach $\chi \sim 80^\circ$ in the alloy with $y = 1.00$ (Fig. 6). The mean β_i rotation angles through Sn-filled hexagonal prisms - related to the Yb-filled ones by a shift of $b/2$ - are approximately given by $\beta_i \approx 360 \cdot q_y - \chi_i$. Hence, as in HfFe_6Ge_6 -type RMn_6Sn_6 helimagnets, β_i is lower than χ_i and does not exceed $\beta \sim 35^\circ$.

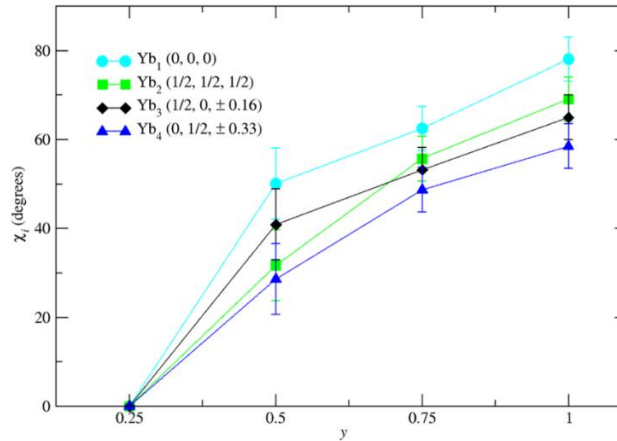


Fig. 6. (color online) Composition dependence of the mean χ_i angles between Mn moments of two hexagonal planes surrounding Yb atoms at 2 K.

4. Discussion and conclusion

We have investigated the Yb valence and local magnetism as well as the magnetic structures in the $\text{YbMn}_{6-y}\text{Fe}_y\text{Sn}_6$ series by means of X-ray absorption techniques (XANES and XMCD) at the Yb L_3 edge and neutron diffraction experiments.

The Fe for Mn substitution leads to a reduction of the Yb valence. This reduction is perceptible at both 300 K (in the paramagnetic state) and 5 K. Consequently, the decrease of the Yb valence cannot be mainly driven by modifications in the $T = \text{Mn/Fe}$ magnetic arrangement. The Yb valence change is opposite to that expected from the chemical pressure increase due to lattice contraction. This suggests the Yb valence change to be of electronic origin, as observed for instance in $\text{YbCu}_{5-x}\text{Ga}_x$ [27].

The Yb valence reduction (at most $\Delta v \sim 0.2$) does not compensate for the increase of valence electrons due to Fe for Mn substitution. Thus, the valence electron concentration increases upon Fe doping, which very likely drives the reinforcement of the antiferromagnetic exchange interactions, as generally observed in 1:6:6 systems. The $y = 0.25$ alloy keeps the ferromagnetism of the ternary YbMn_6Sn_6 parent compound, while a helimagnetic ground state with $\mathbf{k} = 0$, $q_y, 0$ is stabilized in the Fe richer alloys. To refine the neutron data it was necessary to introduce a phase shift between $T = \text{Mn/Fe}$ moments pertaining to the same deformed kagomé plane. This leads to strongly non-collinear alignment of the T moments in a given kagomé plane, which, to the best of our knowledge, had never yet been observed in 1:6:6 systems where the magnetic structures have always been found to be built from ferromagnetic kagomé layers. The rise of antiferromagnetism upon Fe doping also manifests through an enlargement of the temperature range of the helimagnetic state and through an increase of the turn-angle. Further, the higher turn-angle through Yb-filled hexagonal prisms suggests that Yb has a local influence on the exchange couplings. It could be involved in a sort of superexchange interlayer interaction, absent in the Sn-filled hexagonal prisms.

The increase of the turn-angle upon Fe doping yields a reduction of the hybridization induced $5d$ moment on Yb, i.e. a reduction of the exchange field generated by the T sublattice that is expected to be proportional to $\cos \frac{\chi}{2}$. This manifests through the reduction of the dichroic effect at the Yb L_3 edge upon Fe doping (Fig. 3). In Ref. [7], it has been proposed, based on a toy model, that the exchange field due to Mn sublattice may promote trivalency of Yb in $\text{YbMn}_6\text{Ge}_{6-x}\text{Sn}_x$. Although the limited accuracy of the extracted Yb valence values (± 0.02) does not allow us to draw firm conclusion, we note that the room-temperature paramagnetic state Yb valence values are lower than the 5 K values, temperature at which the exchange field is clearly non-zero. This unusual thermal dependence of the Yb valence, at odds to the usual behavior [28], has also been observed in $\text{YbMn}_6\text{Ge}_{6-x}\text{Sn}_x$ [7,8] and in $\text{Yb}_{0.88}\text{Fe}_4\text{Sb}_{12}$ [29]. Further, the Yb valence increase on cooling appears a little more marked for the ferromagnetic $y = 0.25$ alloy with higher H_{ex} than in the helimagnets.

Our work shows again the strong interplay between $3d$ magnetism and the electronic properties of Yb in the $\text{YbMn}_6\text{Ge}_{6-x}\text{Sn}_x$ alloys and their derivatives. In $\text{YbMn}_{6-y}\text{Fe}_y\text{Sn}_6$, the Fe for Mn substitution leads to modification of the electronic structure of the alloys such that the Yb valence decrease. It also promotes antiferromagnetic interactions within the $3d$ sublattice that lower the hybridization induced $5d$

moment on Yb. High temperature signatures of quantum criticality is one of the singular physical behaviors that have already been evidenced in this family of alloys [10]. In $\text{YbMn}_{6-y}\text{Fe}_y\text{Sn}_6$, the Yb magnetic instability and the corresponding quantum critical point could be crossed by using external pressure or by Ge doping. The temperature extent of the quantum critical effects is expected to reduce with the exchange field.

Acknowledgments

We are indebted to the Institut Laue Langevin, Grenoble, France (exp. N° 5-31-2509) and to the synchrotron SOLEIL, Saint-Aubin, France (exp. N° 20170707) for the allocated beam time.

References

- [1] S. Wirth and F. Steglich, *Nat. Rev. Mat.* 1 (2016) 16051.
- [2] H. Zhao, J. Zhang, M. Lyu, S. Bachus, Y. Tokiwa, P. Gegenwart, S. Zhang, J. Cheng, Yi-f. Yang, G. Chen, Y. Isikawa, Q. Si, F. Steglich, and P. Sun, *Nat. Phys.* 15 (2019) 1261.
- [3] P. Cha, N. Wentzell, O. Parcollet, A. Georges, and E.-A. Kim, *PNAS* 117 (2020) 18341.
- [4] H. v. Löhneysen, A. Rosch, M. Vojta, P. Wölfle, *Rev. Mod. Phys.* 79 (2007) 1015.
- [5] E. Morosan, D. Natelson, A.H. Nevidomskyy, and Q. Si, *Adv. Mater.* 24 (2012) 4896.
- [6] T. Mazet, H. Ihou-Mouko, D.H. Ryan, C.J. Voyer, J.M. Cadogan, B. Malaman, *J. Phys. Condens. Matter* 22 (2010) 116005.
- [7] T. Mazet, D. Malterre, M. François, C. Dallera, M. Grioni, G. Monaco, *Phys. Rev. Lett.* 111 (2013) 096402.
- [8] T. Mazet, D. Malterre, M. François, L. Eichenberger, M. Grioni, C. Dallera, G. Monaco, *Phys. Rev. B* 92 (2015) 075105.
- [9] L. Eichenberger, D. Malterre, B. Malaman, T. Mazet, *Phys. Rev. B* 96 (2017) 155129.
- [10] L. Eichenberger, A. Magnette, D. Malterre, R. Sibille, F. Baudelet, L. Nataf, and T. Mazet, *Phys. Rev. B* 101 (2020) 020408(R).
- [11] S.G. Sankar, V.U.S. Rao, E. Segal, W.E. Wallace, W.G.D. Frederick, and H.J. Garrett, *Phys. Rev. B* 11 (1975) 435.
- [12] T. Mazet and B. Malaman, *J. Alloys Compd.* 325 (2001) 67.

- [13] O. Cakir, I. Dincer, E. Duman, T. Krenke, A. Elmali, Y. Elerman, J. Alloys Compd. 441 (2007) 19.
- [14] L. Eichenberger, G. Venturini, B. Malaman, L. Nataf, F. Baudalet, T. Mazet, J. Alloys Compd. 695 (2017) 286.
- [15] A. Magnette, A. Vernière, G. Venturini, L. Eichenberger, B. Malaman, T. Mazet, J. Magn. Mater. 458 (2018) 19.
- [16] B. Chafik El Idrissi, G. Venturini and B. Malaman, Mat. Res. Bull. 26 (1991) 1331.
- [17] T. Mazet, R. Welter, B. Malaman, J. Magn. Mater. 204 (1999) 11.
- [18] F. Baudalet, L. Nataf, and R. Torchio, High Pressure Res. 36 (2016) 429.
- [19] J. Rodríguez-Carvajal, Phys. B 192 (1993) 55.
- [20] L.B. McCusker, R.B. Von Dreele, D.E. Cox, D. Louër and P. Scardi, J. Appl. Crystallogr. 32 (1999) 36.
- [21] E. Beaurepaire, H. Bulou, F. Scheurer, J.P. Kappler, Magnetism and Synchrotron Radiation, Springer-Verlag, Berlin Heidelberg, 2010.
- [22] K. Fukui, H. Ogasawara, A. Kotani, I. Harada, H. Maruyama, N. Kawamura, K. Kobayashi, J. Chaboy, and A. Marcelli, Phys. Rev. B 64 (2001) 104405.
- [23] T. Mazet, O. Isnard, and B. Malaman, J. Phys.: Condens. Matter 17 (2005) 1547.
- [24] E.V. Rosenfeld, N.V. Mushnikov, Physica B 403 (2008) 1898.
- [25] J.M. Hastings, L.M. Corliss, Phys. Rev. 126 (1962) 556.
- [26] N.M. Belyavina and V. Ya. Markiv, Dopov. Akad. Nauk. Ukr. RSR Ser. B12 (1982) 30.
- [27] E. Bauer, Le Tuan, R. Hauser, E. Gratz, T. Holubar, G. Hilscher, H. Michor, W. Perthod, C. Godart, E. Alleno, K. Hiebl, Phys. Rev. B 52 (1995) 4327.
- [28] N.E. Bickers, D.L. Cox, and J. Wilkins, Phys. Rev. B 36 (1987) 2036.
- [29] H. Yamaoka, I. Jarrige, N. Tsuji, J.-F. Lin, T. Ikeno, Y. Isikawa, K. Nishimura, R. Higashinaka, H. Sato, N. Hiraoka, H. Ishii, and K.-D Tsuei, Phys. Rev. Lett. 107 (2011) 177203.